ACS NANO

www.acsnano.org

ARTICLE

# Shearmetry of Fluids with Tunable Rheology by Polarized Luminescence of Rare Earth-Doped Nanorods

Zijun Wang, Qilin Zou, Lilian Magermans, Gabriel Amselem, Claire A. Dessalles, Bruno Louis, Marcel Filoche, Thierry Gacoin,* and Jongwook Kim*

Cite This: https://doi.org/10.1021/acsnano.4c09493

Read Online

ACCESS | Metrics & More | Article Recommendations | Supporting Information

**ABSTRACT:** **Shear stress plays a critical role in regulating physiological processes within microcirculatory systems. While particle imaging velocimetry is a standard technique for quantifying shear flow, uncertainty near boundaries and low resolution remain severe restrictions. Additionally, shear stress determination is particularly challenging in biofluids due to their significant non-Newtonian behaviors. The present study develops a shearmetry technique in physiological settings using a biomimetic fluid containing rare earth-doped luminescent nanorods acting in two roles. First, they are used as colloidal additives adjusting rheological properties in physiological media. Their anisotropic morphology and interparticle interaction synergistically induce a non-Newtonian shear-thinning effect emulating real biofluids. Second, they can probe shear stress due to the shear-induced alignment. The polarized luminescence of the nanorods allows for quantifying their orientational order parameter and thus correlated shear stress. Using scanning confocal microscopy, we demonstrate the tomographic mapping of the shear stress distribution in microfluidics. High shear stress is evident near the constriction and the cellular periphery, in which non-Newtonian effects can have a significant impact. This emerging shearmetry technique is promising for implementation in physiological and rheological environments of biofluids.**

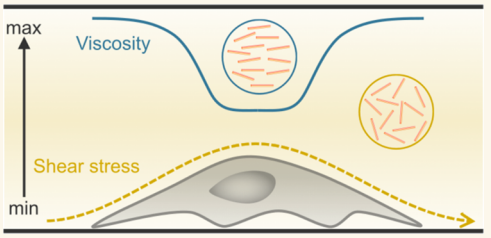


**KEYWORDS:** *rare earth, nanorod, polarization, spectroscopy, microfluidics, non-Newtonian fluid, shear stress*



Most human cells are surrounded by specific fluids such as blood, lymph, periciliary liquid, or mucus. The shear stress ($\tau$) induced by the flow of these biofluids regulates various physiological processes including gene expression, proliferation, and the transport of nutrients and waste products.[1,2] For instance, endothelial cells lining blood vessels are primarily affected by blood flow due to their direct contact with the bloodstream.[3−5] Certain epithelial cells such as intestinal cells and pulmonary cells in the respiratory tract are also subject to shear stress.[6−8] Consequently, accurate assessment and quantification of the shear stress exerted by biofluidic flows on cells are crucial to understanding their mechanobiological response in terms of activity (*e.g.*, gene expression and path activation) and morphology.

In this perspective, microfluidics provides highly efficient tools to develop on-chip platforms and analyze complex phenomena emerging from the interaction between flows and cells or cell cultures in controlled environments. This advancement leads to increasingly realistic models of biological functions.[9] A key feature of such advancement is the ability to reproduce the flow conditions that physiological fluids experience in living organisms, accurately replicating their rheological properties, such as non-Newtonian behavior. For example, blood presents a shear-thinning property as red blood cells can deform and aggregate reversibly under shear stress.[10,11] This non-Newtonian property is paramount for blood flow through narrow capillaries, yet it poses challenges for precise shear stress measurement.[12,13] In practical microfluidic experiments, complex rheological behaviors such as the shear-thinning characteristics of blood or the yield-stress fluid behavior of mucus are often reproduced by the use of polymeric solutions with varying concentrations.[14,15]

In all of these setups, accurately measuring the local flow properties, in particular the shear stress either internally or against the cellular wall, remains a major issue. Earlier computational studies simulating shear profiles on cultured living cells[16,17] highlighted the need for experimental techniques capable of measuring local shear, which varies

Received: July 16, 2024
Revised: September 27, 2024
Accepted: October 4, 2024

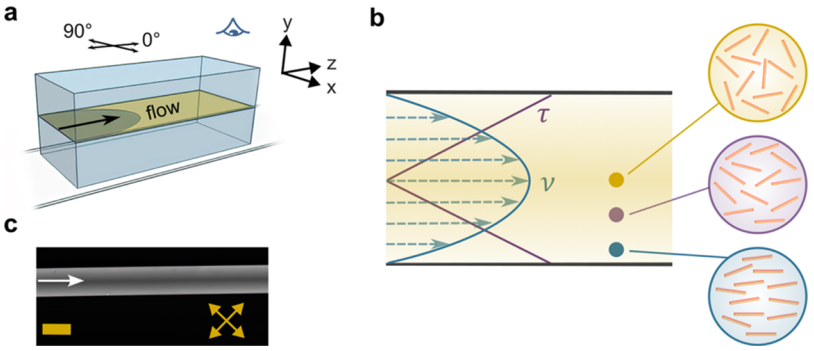


**Figure 1. Orientation of nanorods under flow in a straight microfluidic channel. (a) Schematic illustration of the experiment using a straight square-shaped microchannel showing a typical Poiseuille flow profile in the horizontal midplane. A polarizing analyzer is rotated at an angle of 0 or 90° (parallel or perpendicular to the flow direction). A 3D coordinate is used with the *x*-axis along the channel width, the *y*-axis along the height, and the *z*-axis along the flow direction. The observation direction is along the *y*-axis. (b) Velocity ($\nu$) and shear stress ($\tau$) profiles of a Poiseuille flow resulting in different degrees of orientation of nanorods depending on the varied local shear stress in the horizontal midplane. (c) Top view of the flow birefringence in the microchannel with a square cross-section (50 $\mu$m × 50 $\mu$m) of saline solution containing the $LaPO_4$/Eu nanorod (volume fraction = 1.8 vol %) with a flow rate of 1.8 $\mu$L/min. The channel was placed horizontally between two crossed polarizers with ±45° angles. The scale bar is 50 $\mu$m.**

sensitively with the continuous morphogenesis of the cells. Currently, the standard experimental methods for quantifying the flow characteristics are particle imaging velocimetry (PIV)[18,19] and particle tracking velocimetry (PTV).[20−22] They work by capturing images of tracer particles dispersed in the fluid and analyzing the frames with cross-correlation algorithms to determine the flow velocity ($\nu$) profile. Although PIV/PTV is a well-developed technique, the principle based on measuring the velocity has certain limitations, especially when the interest lies in the shear stress. To obtain the shear stress, the velocity field obtained by an interpolation of discrete data points must be differentiated, which amplifies noise and inaccuracies. Also, the measurement accuracy drops near the walls where the velocity almost vanishes, while wall shear or interfacial shear is often of the highest interest in biofluidic systems.[23,24] Furthermore, the spatial and temporal resolutions of velocimetry trade off against each other by principle. Due to these limitations, previous attempts to use PIV for mapping the distribution of the shear stress near cells often lack accuracy on a subcellular scale.[25]

We introduce here a technique that combines the tunability of fluid rheology with a recently demonstrated methodology of shearmetry based on the polarized luminescence property of $Eu^{3+}$-doped lanthanum phosphate ($LaPO_4$/Eu) nanorods.[26] The principal idea employs rheo-optics,[27] which was extensively studied earlier through the observation of flow birefringence in polymers as well as colloids like the tobacco mosaic virus.[28] Rod-shaped nanoparticles dispersed in a fluid tend to orient along the flow shear.[29] The collective orientation of an ensemble of nanorods can be obtained by analyzing their polarized emission spectra, from which the magnitude and direction of shear can be determined. This allows for an instantaneous and spatially resolved measurement of shear without tracking individual tracers. For applications in biofluid-containing salts and macromolecules that significantly affect the dynamics of nanorods,[30] the $LaPO_4$/Eu surface needs to be functionalized with specific zwitterionic polymer ligands, achieving superior colloidal stability in the physiological environments compatible with diverse human cells.[31−33] A remaining challenge is adaptation to the various rheological behaviors of biofluids: the concentrated ionic, molecular, and cellular contents cause complex rheology, which can be further modified by the addition of nanoparticles.[34]

In this work, we focus on assessing the non-Newtonian property of our $LaPO_4$/Eu nanorod suspension and establishing reliable cellular shearmetry. We first quantify the shear-thinning effect induced by the colloidal dispersion of the nanorods within an aqueous saline medium used as a model fluid system mimicking non-Newtonian biofluids. This measurement serves to establish a calibration curve, which correlates the shear stress with the orientation of nanorods. A broad range of shear sensitivity is achieved through the manipulation of various parameters including nanorod concentration, dispersion medium, and viscosity. We then perform a shear measurement in a microfluidic channel featuring curved streamlines in the presence of either an artificial constriction or living cells. By employing scanning confocal microscopy, we are able to reconstruct maps of the shear stress distribution on cross-sectional areas of the microfluidic channel from the nanorod-induced polarization spectroscopy. High shear stress is found in the vicinity of cellular surfaces as they act like constrictions, which substantiates the applicability of our shearmetry technique in diverse mechanobiological studies.

## RESULTS AND DISCUSSION

**Nanorod Orientation in a Microfluidic Channel.** The $LaPO_4$/Eu nanorods were prepared by the previously reported hydrothermal synthesis method.[31,35] A sulfobetaine-phosphonate block zwitterionic copolymer was functionalized on the nanorod surface to enable dispersion in physiological media.[32] The nanorods are 150 nm in length ($l$) and 4 nm in diameter ($d$) on average. The nanorod suspension is then flowed in a straight microfluidic channel with a square cross-section, as schematically shown in Figure 1a. Additional details on device fabrication and experimental conditions can be found in the Supporting Information (S.I.).

Figure 1b displays the expected tendency of the nanorod orientation depending on the locally applied shear stress. It is worth noting that the microscopic focal volume (on the order of $\mu m^3$) contains hundreds of nanorods. Therefore, the observed optical signal represents a statistical average of the nanorod ensemble. In the ideal case of a Newtonian fluid, the


https://doi.org/10.1021/acsnano.4c09493
ACS Nano XXXX, XXX, XXX−XXX

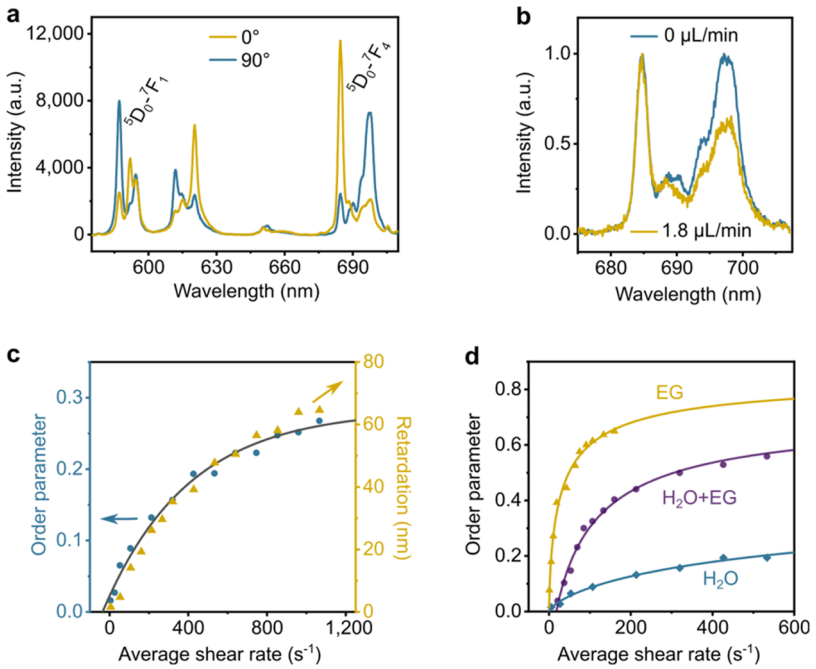


**Figure 2. Correlation between polarized luminescence and average shear rate. (a) Reference polarized emission spectra of perfectly aligned $LaPO_4$/Eu nanorods in liquid-crystalline assembly with the polarizer parallel and perpendicular to the rod orientation. (b) Flow rate-dependent polarized emission spectra for the $^5D_0$–$^7F_4$ ED transition observed with the polarizer parallel to the flow direction (0°). (c) Order parameter calculated from the polarized luminescence and measured optical retardation from birefringence as a function of the average shear rate. The curve is a guide line fitted with an exponential function. (d) Calculated order parameters of nanorod suspensions in water, ethylene glycol (EG), and their mixture (equal volume of $H_2O$ and EG) as a function of average shear rate. The volume fraction of nanorods is 1.2 vol % in all cases. Note that the average shear rate is calculated *via* $4Q/wh^2$ based on the Newtonian assumption.**

flow velocity profile at the middle height of the square channel should follow a parabolic profile, as found in the standard Poiseuille flow. The wall shear rate is defined by $6Q/wh^2$, where $Q$, $w$, and $h$ represent the flow rate, channel width, and height, respectively. The average shear rate ($\dot{\gamma}$) through the whole channel is $4Q/wh^2$. The shear stress ($\tau = \mu \cdot \dot{\gamma}$ with $\mu$ as the dynamic viscosity of a fluid, which remains constant for Newtonian fluids) should linearly increase from 0 at the center to a maximum at the wall.[36] Shear stress applies torque to the nanorods, causing their rotation to the direction of flow. This rotation is counterbalanced by thermal diffusion, which randomizes their orientation.[37] Therefore, the local degree of orientation of the rods, quantified as the order parameter ($f$, Figure S1), increases from 0 (random orientation) at the center to a maximum value of 1 (perfect orientation) when the rods approach the wall. As the nanorods align, the suspension's optical properties change and are characterized by birefringence. Under crossed polarizers, the flow birefringence ($\Delta n \propto f$)[37,38] appears as bright near the walls and dark at the center (Figure 1c), demonstrating the expected tendency of nanorod alignment.[38,39]

**Shear-Optical Calibration.** To quantitatively determine the order parameter less than 1, reference luminescence spectra are needed from perfectly aligned nanorods ($f = 1$). These reference spectra can be obtained from the liquid-crystalline self-assembly of the nanorods (Figure S2) with the order parameter close to 1,[40] displaying the characteristic $Eu^{3+}$ emission lines (Figure 2a). They attribute to the magnetic dipole transition (MD, $^5D_0$–$^7F_1$) and the forced electric dipole transition (ED, $^5D_0$–$^7F_{2,3,4}$).[41] The MD lines at 587 and 592 nm and ED lines at 685 and 698 nm ($^5D_0$–$^7F_4$), characterized by high degrees of polarization (defined by $(I_{max} - I_{min})/(I_{max} + I_{min})$, where $I_{max}$ and $I_{min}$ represent the maximum and minimum luminescence intensities while rotating the polarizer) ranging from 0.5 to 0.8, are chosen for the analysis of order parameter. When the nanorods are partially oriented under flow ($0 < f < 1$), the relative intensities of different lines vary with the flow rate (Figure 2b). This variation allows for the order parameter calculation (the calculation method using the reference spectra is provided in the S.I.). By gradually changing the flow rate in the straight channel and conducting optical measurements, we are able to calibrate the order parameter versus the average shear rate. Figure 2c illustrates the $f$–$\dot{\gamma}$ dependency, which aligns with the trend of optical retardation ($\Delta n \cdot h$) obtained through birefringence measurements.

To investigate the effect of fluid viscosity, calibration functions ($f$ *vs* $Q$) were established for the same nanorods dispersed in different media: water, ethylene glycol, and a mixture of the two (Figure 2d). The dynamic viscosity of ethylene glycol is 16.1 mPa·s, an order of magnitude higher than that of water (1.0 mPa·s).[42] It is evident that the nanorods exhibit stronger alignment when the medium viscosity is higher, providing evidence of a direct correlation between the order parameter and shear stress. Technically, this result demonstrates that the experimental sensitivity range to the shear rate or flow rate can be adjusted by varying the medium viscosity. Furthermore, tuning the shear sensitivity is achievable by changing the volume fraction of nanorods as reducing interparticle distance increases interparticle interaction (Figure S3). We find that in diluted aqueous media (*e.g.*, 1.0 vol %), the order parameter is linearly sensitive to the average shear rate below 1000 s$^{-1}$. By increasing the viscosity


https://doi.org/10.1021/acsnano.4c09493
ACS Nano XXXX, XXX, XXX–XXX

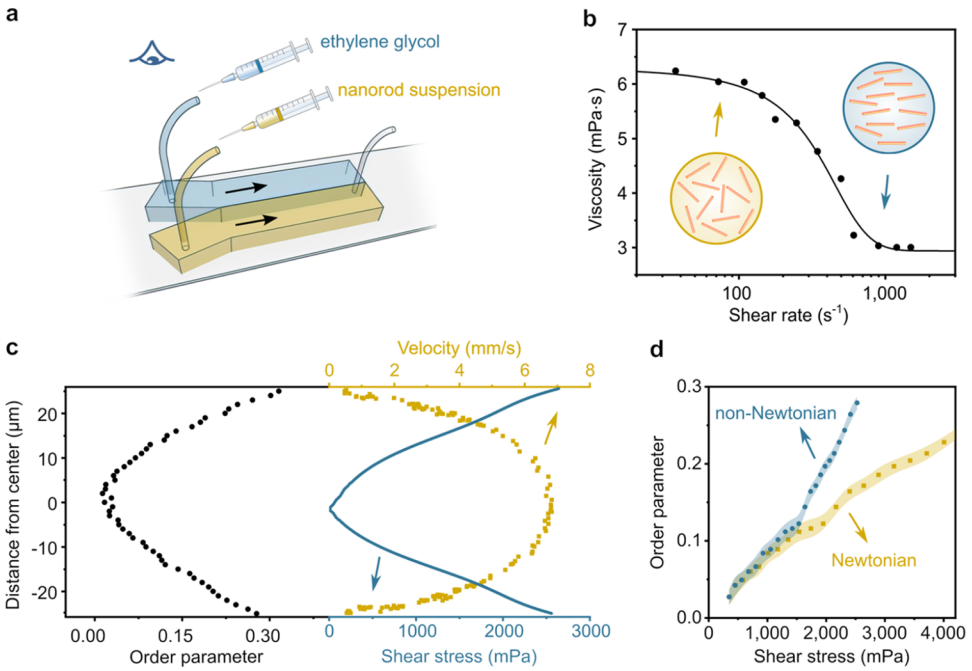


**Figure 3. Calibration of the non-Newtonian shear-thinning behavior. (a) Schematic illustration of a Y-shaped microfluidic channel for the viscosity measurements of the nanorod suspension (1.8 vol % in saline) flowed together with pure ethylene glycol with known viscosity. The detector is on the top of the channel to observe the fluid interface in the horizontal midplane. (b) Measured viscosity of the saline suspension as a function of shear rate showing a shear-thinning effect. The insets display the varying degrees of nanorod orientation at different shear rates. The curve is a guide to the eye. (c) Profiles of order parameter calculated with polarized luminescence, velocity measured by PTV, and local shear stress in the horizontal midplane ($y$-axis corresponds to the direction of channel width) at a flow rate of 1 $\mu$L/min. The shear rate is derived from the velocity profile using interpolation. (d) Calibration curve of order parameter as a function of shear stress under the actual non-Newtonian and assumed Newtonian ($\mu$ = 6.2 mPa·s) conditions. The colored areas denote the standard deviation of the measurements.**

in medium, the $f-\dot{\gamma}$ sensitive range narrows, but the sensitivity significantly increases (evidenced by the steeper slopes).

**Non-Newtonian Calibration.** One should proceed to examine the rheological properties of the nanorod suspensions. Besides the interest in understanding them on a fundamental level, this knowledge is important for optimizing the accuracy of shearmetry. We measured the dynamic viscosity of the nanorod suspension flowing in parallel to pure ethylene glycol in a Y-shaped microfluidic channel (Figure 3a).[43] The methodology and results of the measurement are presented in Figures S4 and S5. The obtained $\mu-\dot{\gamma}$ relationship (Figure 3b) reveals a significant shear-thinning effect in the nanorod suspension. The viscosity drops from 6.2 to 3.0 mPa·s as the shear rate increases to 1000 s$^{-1}$, a behavior akin to that of blood ($\mu$ = 3.5−10 mPa·s).[13,23] In this sense, our nanorod suspensions can mimic certain non-Newtonian biofluids.

This shear-thinning effect is expected when anisotropic particles are involved.[29] In our case, the presence of colloidal nanorods induces a significant non-Newtonian shear-thinning behavior due to the relative orientation of the nanorods and the resulting particle interaction.[12,34] While our surface-modified nanorods can be dispersed in real biofluids, the colloidal parameters (*e.g.*, nanorod concentration, surface chemistry, medium, and ionic strength) can be further adjusted to fine-tune the rheological properties of the suspension. For instance, ethylene glycol suspensions of nanorods also exhibit shear-thinning effects (1.2 vol % in Figure S6). The nanorod concentration dramatically impacts the initial viscosity determining the amplitude of shear-thinning behavior down to the terminal viscosity, which is close to that of the pure medium.

Regarding the shear-thinning property of nanorod suspensions, the above $f-\dot{\gamma}$ calibration functions (Figure 2c,d) are indeed not valid. The viscosity of suspension can vary at different positions within the channel. This requires spatially resolved measurements to establish the $f-\dot{\gamma}$ correlation. The local measurements of polarized luminescence and shear profiles of the nanorod suspension were performed in the horizontal midplane of the straight channel, while PTV was employed to locally quantify the corresponding shear rate. Figure 3c plots the order parameter (more plots at different flow rates are shown in Figure S7) through analyzes of polarization spectra under a confocal microscope (with a focal volume of ∼0.5 $\mu$m$^3$, the optical setup is shown in Figure S8) and the corresponding velocity profile determined by PTV velocimetry at a flow rate of 1 $\mu$L/min. The velocity profile is extracted through a time-correlated analysis, tracking the trajectories of individual beads (Figure S9). The derivative of the velocity profile yields the shear rate, as depicted in Figure S10. This, combined with the shear rate-dependent viscosity (Figure 3b), results in the shear stress profile. The nonlinearity of the shear rate and shear stress profiles further substantiates the deviation from Newtonian behavior for the nanorod suspensions. Subsequently, the local correlation between the order parameter and shear stress can be established by considering the shear-thinning effect. As illustrated in Figure 3d, the $f-\tau$ function is almost linear. Thanks to the shear-thinning effect, the slope is steeper over shear stress of 1600 mPa, suggesting enhanced shear stress sensitivity. The $f-\tau$


https://doi.org/10.1021/acsnano.4c09493
ACS Nano XXXX, XXX, XXX−XXX

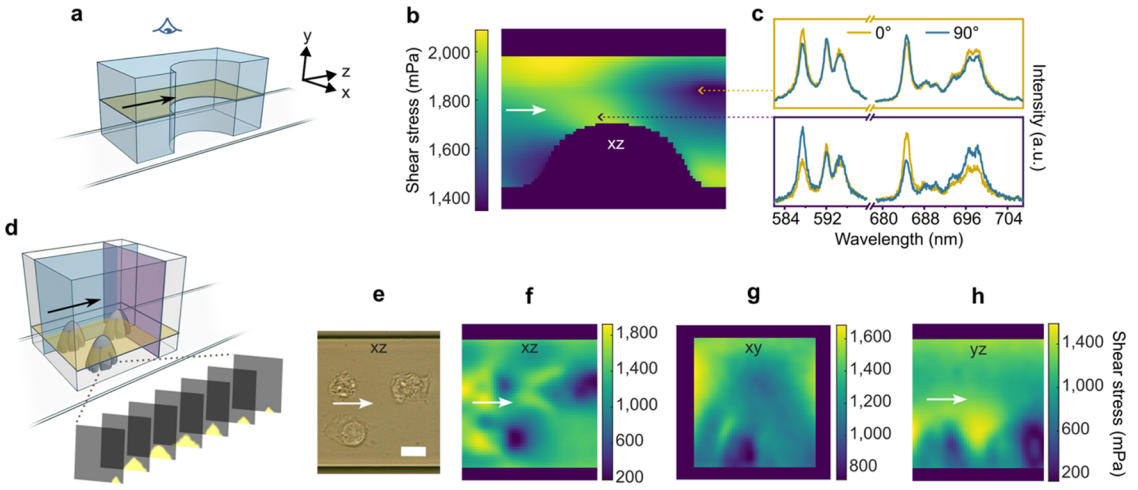


**Figure 4. Shear stress tomography in microfluidics. (a) Schematic illustration of a square channel with an artificial semicircular constriction (radius = 25 $\mu$m) using the identical detection configuration and 3D coordinate. (b) Shear stress map in the horizontal midplane calculated by the presented method for realistic non-Newtonian conditions. (c) Polarized emission spectra obtained from the marked regions with high shear stress near the constriction and low shear stress in the center. (d) Schematic illustration of the orthogonal channel sections, where the shear stress maps were obtained across the human alveolar epithelial A549 cancer cells cultured on the bottom substrate. The series of images at the bottom display cross-sectional slices of a single cell processed by thresholding of luminescence intensity maps. (e) Optical microscopy image of the three cultured cells adhered to the substrate before applying flow. The scale bar indicates 10 $\mu$m. (f-h) Shear stress maps in the orthogonal xz, xy, and yz sections schematized in part (d). The xz section is at a height of 10 $\mu$m above the substrate. In all cases, the saline suspension at 1.8 vol % is flowed at a flow rate of 0.2 $\mu$L/min.**

relation significantly deviates over shear stress of 1000 mPa (≥10% deviation) between the Newtonian assumption and the non-Newtonian case. The shear stress overestimation without shear-thinning calibration can reach as high as 96%. Using this calibration curve, our shearmetry is able to measure shear stress from 200 to 2500 mPa with enhanced sensitivity across this range. This large range includes typical shear stress levels found in most physiological environments (on the order of $10^2$–$10^3$ mPa).[2,4,7] Due to measuring errors, the calculated shear stress can fluctuate and our shearmetry is not accurate if the shear stress is lower than 200 mPa, such as in the case of beating cilia.[20]

**Shear Stress Tomography.** In Figure 4, we present the shearmetry analyses performed based on the newly established $f$–$\tau$ correlation. First, artificial constrictions in a semicircular shape were designed to induce curved streamlines mimicking various circumstances in physiological flows, such as vessel geometry, formed thrombi, and deployed stents.[3,44,45] As schematically illustrated in Figure 4a, the constrictions were constructed vertically along the y direction. We conducted scanning confocal microspectroscopy on the horizontal midplane with the polarizer angles of 0 and 90° while steadily flowing the nanorod suspension through the channel. The spectrographs collected at each point determine the order parameter, which is then transformed into a local shear stress using the $f$–$\tau$ calibration curve (Figure 3d, see the methodology in the S.I.).

On the 2D shear stress maps in the presence of the constriction for a non-Newtonian fluid (Figure 4b), shear stress gradually increases from the center toward the walls as anticipated from the shear stress profile (Figure 3c). The shear stress increase near the constriction is clearly due to the narrowing of the channel width. The regions of high and low shear stress are also spectroscopically demonstrated in Figure 4c, which displays the polarized luminescence spectra (arrows in Figure 4b). Meanwhile, we observe an asymmetric profile of the calculated shear stress map in the up- and downstream regions of the constrictions. A theoretically expected shear stress profile of a viscous microflow is perfectly symmetric across the constriction. We have earlier observed a more significant distortion of the shear rate map in our preliminary study using unfunctionalized and surface-charged nanorods in a nonphysiological medium.[26] It was verified that this asymmetric shear profile originates from the rotational delay in the response of nanorods to the varying direction and strength of shear across the constriction. This delay can be estimated with Peclet number, $Pe = \nu/hD_r$, where $D_r$ is the coefficient of rotational diffusion due to the Brownian motion.[46,47] A lower $Pe$ value leads to less delay as it indicates faster rotational dynamics compared to the advection.[26] The current results using ligand-functionalized nanorods in the physiological medium (Figure 4b) show a significantly reduced extent of distortion compared to the previous results obtained using charged nanorods.[26] We attribute this improvement to the reduced interparticle repulsion in the current system, resulting in a decreased $Pe$ value of 0.2 (discussion in detail in the S.I. and Figure S11). The presented experiments were conducted at room temperature ($T \sim 24$ °C). As $D_r$ is proportional to $k_BT$,[46] the $f$–$\tau$ calibration function should be obtained at the same temperature set for different physiological environments.

Finally, we conducted *in vitro* experiments to demonstrate the applicability of our shearmetry at the single-cell level. The minimal biotoxicity and nonspecific binding of our zwitterion-functionalized nanorods were experimentally demonstrated in our previous work.[32] Human alveolar epithelial A549 cancer cells were cultured in the same type of straight microchannel (Figure 4d,4e, see the details on cell culture and experimental conditions in the S.I.).[48] The cells adhered to the bottom substrate, creating 3D constrictions (height of ~15 $\mu$m revealed by the 3D reconstruction of one cell in the S.I. movie). Figure 4f-h presents calculated shear stress maps on


https://doi.org/10.1021/acsnano.4c09493
ACS Nano XXXX, XXX, XXX−XXX

the three orthogonal scanning sections (Figure 4d) intersecting the cells, revealing an elevated shear stress near the cell surface due to the constricted geometry of the cells.

Enhanced shear stress is particularly evident upstream of each cell, where the streamline should bend quickly (Figure 4f, 4h). Additionally, a notable increase in shear stress is observed near the left channel wall adjacent to the cell (Figure 4g). The shear stress in the vicinity of cells is found in the range of 1200−2000 mPa, which has been known to be significant enough to modify cellular morphology and to trigger various intracellular responses.[49,50] A549 cancer cells are known to be relatively flexible,[51] and we indeed observed slight changes in cell morphology while maintaining their locations after hours of flow (Figure S12). Meanwhile, the fore-aft asymmetric feature is also visible in this measurement with the cells. It is therefore necessary to further improve and optimize the technique to achieve more accurate shear stress maps, eliminating such artifacts. We are currently addressing these major error sources by developing more advanced colloidal systems with a higher rotational diffusion coefficient and by improving confocal resolution in continuous volumetric sample media.

To our knowledge, this is the first tomographic visualization of shear stress directly and locally measured around living cells *in vitro*. This result demonstrates that our shearmetry method is capable of mapping shear stresses in biomicrofluidic systems, promising its application to further studies to unveil various mechanobiological processes that are triggered by flow shear stress. The advantages of this shearmetry technique include potentially high spatial resolution ($\lesssim 1\ \mu m^3$) and short luminescence acquisition time on one spot ($\lesssim 50$ ms) that are limited only by the optical performance of the confocal setting. Therefore, instead of spatially scanning the sample, it is possible to perform real-time and local monitoring of shear dynamics in unsteady flows. We have shown a specific case where the nanorod suspension emulates the non-Newtonian shear-thinning property of blood. The rheology of nanorod suspension can be further controlled to emulate different types of biofluids with varied viscosity and extent of shear-thinning property by careful adjustments of the nanorod concentration and dispersion medium. Hence, the presented method of shearmetry is widely applicable to various biofluidic systems.

## CONCLUSIONS

In summary, this work introduces a shearmetry technique for monitoring the local shear stress in biofluids with high spatiotemporal resolution and real-time observation. By using colloidal nanorods with polarized optical properties and an integrated algorithm, we establish a direct correlation between the shear stress and optical emission. Notably, in the high shear stress region that crucially regulates biological responses, we identify and explain the non-Newtonian properties of the nanorod suspensions. This offers the potential to mimic biofluids and allows for extensive adjustments. We demonstrate the effectiveness of shearmetry in visualizing shear stress distribution in microfluidics with complex constrictions and living cells. The presence of constrictions and cells leads to increased shear stress. The current study represents a significant advancement in achieving a more precise and comprehensive understanding of shear stress in complex biofluids. With further development in nanomaterials, this shearmetry technique holds promise for a wide range of biological and microfluidic applications.

## METHODS

**Fabrication of Microfluidics.** There are two types of microfluidic channels: Y-shaped channels for calibration and straight channels with constrictions for the shearmetry measurements, respectively. The first step involved creating molds for Y-shaped channels as follows: A layer of photoresist film was laminated onto cleaned coverslips by using a laminator (Peak High Speed, PHS-330) at 100 °C. A printed photomask of the designed Y-shaped channels was then positioned on top, and the assembly was exposed to UV light for 15 s. Subsequently, the uncured photoresist was etched by immersing the coverslip in a potassium carbonate (2% by mass) solution for 5−10 min under gentle stirring. Then, the coverslip with a cured photoresist was rinsed with pure water and dried. A second round of UV exposure was performed to further cure the photoresist.

The next step was the fabrication of polydimethylsiloxane (PDMS) channels based on the mold using soft lithography. SYLGARD 184 silicone elastomer base and a curing agent at the volume ratio of 10:1 were mixed thoroughly, degassed, and cast onto the channel mold. PDMS was solidified by heating at 70−80 °C for 5−6 h and then peeled off and cut with a hole punch to create inlet and outlet ports. The cleaned coverslips or glass slides together with cut PDMS were treated with plasma (PDC-002-CE Harrick Plasma) for 60 s. Finally, the channels were formed by attaching PDMS to the substrates. To strengthen the adhesion of the interface, the devices were treated at 90 °C overnight. Straight channels with constrictions were fabricated by using a master mold on a silicon wafer (MicruX Technologies).

**Averaging Measurements of Birefringence and Polarized Emission Spectra.** Nanorod suspensions in a 100 $\mu$L SGE syringe were injected through polyethylene tubing (0.38 mm for the inner diameter and 1.09 mm for the outer diameter, Instech) and a Luer stub with a blunt tip (0.20 mm for the inner diameter and 0.41 mm for the outer diameter, Instech) into microfluidic channels. A KDS syringe pump ensured steady flow at controlled rates. Birefringence was observed on a polarizing optical microscope (Olympus BX51WI, 10× objective, numerical aperture NA = 0.3) with a white-light halogen bulb (100 W) and two crossed polarizers. A charge-coupled device (CCD) camera (Discovery DTA 1600E) captured the images. Polarized emission spectra were measured by using a continuous-wave mode fiber-coupled 394 nm diode laser (OXXIUS) and a monochromator (SpectraPro-300i, Acton Research) coupling with a CCD camera (PIXIS 400, Teledyne Princeton Instruments).

**Line Scan and Shear Stress Tomography.** High-resolution scanning was conducted using a homemade confocal optical microscope based on a Nikon Eclipse Ti-DH microscope. The excitation beam, emitted by the 394 nm laser, was reflected by a long-pass dichroic mirror to focus on an oil immersion objective (60x, NA = 1.4). Emission transmitted by the long-pass dichroic mirror was passed through a 50 $\mu$m pinhole and a rotating half-wave plate before reflecting by a polarizing beam splitter to a monochromator (IsoPlane SCT-320, Teledyne Princeton Instruments) and electron multiplying CCD camera (ProEM+: 1600 EMCCD, Teledyne Princeton Instruments). The scanning piezo stage was synchronized with the half-wave plate, monochromator, and EMCCD camera through a central processor and software developed by Inscoper. For scanning measurements, one pixel corresponded to a square of 1 $\mu$m side length, and the acquisition time was 50 ms. After the data collection, polarized emission spectra (three polarizer angles at 0, 45, and 90°; see the details on the equations in the S.I.) were analyzed using custom Matlab and Python codes to determine local shear stress.

**Viscosity Measurements.** Two media, including one with known viscosity (using pure ethylene glycol) and the nanorod suspension under study (1.8 vol % in saline or 1.2 vol % in ethylene glycol), were pumped separately by two Cetoni Nemesys syringe pumps into the two inlets of the Y-shaped microfluidic channel. We kept the same flow rate for both media and gradually increased the rate. The interface where the two media merged was imaged by a Nikon Eclipse Ti−U microscope (20x objective, NA = 0.45) and a high-speed camera (Photron FASTCAM SA3). Shear rate-dependent viscosity was calculated based on the relative width and flow rate of the two


https://doi.org/10.1021/acsnano.4c09493
ACS Nano XXXX, XXX, XXX−XXX

media. Due to the 3D nature of the channel, the viscosity and corresponding shear rate should be corrected (see the details on the equations and methodology in the S.I.).

**Particle Tracking Velocimetry.** Nanorod suspensions mixed with microbeads (1.75 $\mu$m in diameter, carboxylate functionalization, 0.025%, w/v, Polysciences) were injected into straight microfluidic channels with increased flow rates *via* a Cetoni Nemesys syringe pump. The same Nikon Eclipse Ti−U microscope (40x objective, NA = 0.55) with the high-speed camera recorded a series of images (at a specific frame rate depending on the flow rate) in the horizontal midplane. Trajectories of microbeads were processed using ImageJ and Matlab to determine velocity profiles. Shear rate was then derived from the velocity profile.

**Cell Culture and Microfluidic Experiments.** Human type II alveolar epithelial A549 cells (American Type Culture Collection, Biological Industries) were cultured at 37 °C and 5% $CO_2$ in Dulbecco's Modified Eagle's Medium (DMEM), supplemented with 10% fetal bovine serum, 1% amphotericin B, and 1% penicillin/streptomycin. The cell suspension at a concentration of $2 \times 10^6$ cells/mL was seeded into the microfluidic channel. After two-day incubation (the channel immersed in DMEM) to allow cell attachment, nonadhered cells were flushed with fresh medium. The nanorod suspension was then flowed through the cell-cultured channel for spectroscopic measurements in the confocal microscope.

## ASSOCIATED CONTENT

### Supporting Information

The Supporting Information is available free of charge at https://pubs.acs.org/doi/10.1021/acsnano.4c09493.

Measurement configuration, methodology, optical microscopy images, calibration curves, and viscosity measurements (PDF)

## AUTHOR INFORMATION


### Corresponding Authors

**Thierry Gacoin** − *Laboratoire de Physique de la Matière Condensée, Ecole Polytechnique, CNRS, IP Paris, 91128 Palaiseau, France;* orcid.org/0000-0001-6774-3181; Email: thierry.gacoin@polytechnique.edu

**Jongwook Kim** − *Laboratoire de Physique de la Matière Condensée, Ecole Polytechnique, CNRS, IP Paris, 91128 Palaiseau, France;* orcid.org/0000-0003-0404-6973; Email: jong-wook.kim@polytechnique.edu

### Authors

**Zijun Wang** − *Laboratoire de Physique de la Matière Condensée, Ecole Polytechnique, CNRS, IP Paris, 91128 Palaiseau, France; L'Institut Mondor de Recherche Biomédicale, Université Paris Est Créteil, INSERM U955, CNRS, 94010 Créteil, France*

**Qilin Zou** − *Laboratoire de Physique de la Matière Condensée, Ecole Polytechnique, CNRS, IP Paris, 91128 Palaiseau, France*

**Lilian Magermans** − *Laboratoire de Physique de la Matière Condensée, Ecole Polytechnique, CNRS, IP Paris, 91128 Palaiseau, France*

**Gabriel Amselem** − *Laboratoire d'Hydrodynamique, Ecole Polytechnique, CNRS, IP Paris, 91128 Palaiseau, France;* orcid.org/0000-0003-4563-2899

**Claire A. Dessalles** − *Laboratoire d'Hydrodynamique, Ecole Polytechnique, CNRS, IP Paris, 91128 Palaiseau, France*

**Bruno Louis** − *L'Institut Mondor de Recherche Biomédicale, Université Paris Est Créteil, INSERM U955, CNRS, 94010 Créteil, France*

**Marcel Filoche** − *L'Institut Mondor de Recherche Biomédicale, Université Paris Est Créteil, INSERM U955, CNRS, 94010 Créteil, France; Institut Langevin, ESPCI Paris, PSL University, CNRS, 75005 Paris, France;* orcid.org/0000-0001-8637-3016

Complete contact information is available at: https://pubs.acs.org/10.1021/acsnano.4c09493


### Author Contributions

J.K., T.G., and M.F. developed the concept. Z.W. prepared the nanoparticles. Z.W. and Q.Z. performed the optical measurements. Z.W. fabricated the microfluidic channels and performed the PTV and viscosity measurements. G.A., Z.W., and C.A.D. analyzed the data of PTV and viscosity measurements. Z.W. and B.L. designed and prepared the cells cultured in microchannels. Z.W. and L.M. analyzed the data developing the Matlab and Python codes. Z.W. and J.K. prepared the manuscript. J.K. and T.G. supervised the research. The manuscript was revised through contributions of all authors.

### Notes

The authors declare no competing financial interest.

## ACKNOWLEDGMENTS

We acknowledge INSCOPER for providing the synchronized imaging solution. We are grateful to Virginie Fournier for her help with cell culture. This research was supported by the Medical Research Foundation (DCM20181039556, Chemistry for Medicine program), the Polytechnic Institute of Paris (2020MATU0376), and the French National Research Agency (ANR-19-CE09-0033 and ANR-10-EQPX-0050).

## REFERENCES

(1) Chiu, J.-J.; Chien, S. Effects of Disturbed Flow on Vascular Endothelium: Pathophysiological Basis and Clinical Perspectives. *Physiol. Rev.* **2011**, *91*, 327−387.

(2) Dessalles, C. A.; Leclech, C.; Castagnino, A.; Barakat, A. I. Integration of Substrate-and Flow-Derived Stresses in Endothelial Cell Mechanobiology. *Commun. Biol.* **2021**, *4*, 764.

(3) Davies, P. F. Hemodynamic Shear Stress and the Endothelium in Cardiovascular Pathophysiology. *Nat. Clin. Pract. Cardiovasc. Med.* **2009**, *6*, 16−26.

(4) Shemesh, J.; Jalilian, I.; Shi, A.; Yeoh, G. H.; Tate, M. L. K.; Warkiani, M. E. Flow-Induced Stress on Adherent Cells in Microfluidic Devices. *Lab Chip* **2015**, *15*, 4114−4127.

(5) Campinho, P.; Vilfan, A.; Vermot, J. Blood Flow Forces in Shaping the Vascular System: a Focus on Endothelial Cell Behavior. *Front. Vasc. Physiol.* **2020**, *11*, 552.

(6) Huh, D.; Fujioka, H.; Tung, Y.-C.; Futai, N.; Paine, R., III; Grotberg, J. B.; Takayama, S. Acoustically Detectable Cellular-Level Lung Injury Induced by Fluid Mechanical Stresses in Microfluidic Airway Systems. *Proc. Natl. Acad. Sci. U. S. A.* **2007**, *104*, 18886−18891.

(7) Huh, D.; Matthews, B. D.; Mammoto, A.; Montoya-Zavala, M.; Hsin, H. Y.; Ingber, D. E. Reconstituting Organ-Level Lung Functions on a Chip. *Science* **2010**, *328*, 1662−1668.

(8) Kim, H. J.; Huh, D.; Hamilton, G.; Ingber, D. E. Human Gut-on-a-Chip Inhabited by Microbial Flora that Experiences Intestinal Peristalsis-Like Motions and Flow. *Lab Chip* **2012**, *12*, 2165−2174.

(9) Sebastian, B.; Dittrich, P. S. Microfluidics to Mimic Blood Flow in Health and Disease. *Annu. Rev. Fluid. Mech.* **2018**, *50*, 483−504.

(10) Luo, X.; Kuang, Z. A Study on the Constitutive Equation of Blood. *J. Biomech.* **1992**, *25*, 929−934.

(11) Tomaiuolo, G.; Lanotte, L.; D'Apolito, R.; Cassinese, A.; Guido, S. Microconfined Flow Behavior of Red Blood Cells. *Med. Eng. Phys.* **2016**, *38*, 11−16.
(12) Lu, X.; Liu, C.; Hu, G.; Xuan, X. Particle Manipulations in Non-Newtonian Microfluidics: A Review. *J. Colloid Interface Sci.* **2017**, *500*, 182−201.
(13) Gupta, S.; Wang, W. S.; Vanapalli, S. A. Microfluidic Viscometers for Shear Rheology of Complex Fluids and Biofluids. *Biomicrofluidics* **2016**, *10*, 043402.
(14) Raj M, K.; Priyadarshani, J.; Karan, P.; Bandyopadhyay, S.; Bhattacharya, S.; Chakraborty, S. Bio-Inspired Microfluidics: A Review. *Biomicrofluidics* **2023**, *17*, 051503.
(15) Hu, Y.; Bian, S.; Grotberg, J.; Filoche, M.; White, J.; Takayama, S.; Grotberg, J. B. A Microfluidic Model to Study Fluid Dynamics of Mucus Plug Rupture in Small Lung Airways. *Biomicrofluidics* **2015**, *9*, 044119.
(16) Barbee, K. A.; Mundel, T.; Lal, R.; Davies, P. F. Subcellular Distribution of Shear Stress at the Surface of Flow-Aligned and Nonaligned Endothelial Monolayers. *Am. J. Physiol. Heart Circ. Physiol.* **1995**, *268*, H1765−H1772.
(17) Davies, P. F.; Barbee, K. A.; Volin, M. V.; Robotewskyj, A.; Chen, J.; Joseph, L.; Griem, M. L.; Wernick, M. N.; Jacobs, E.; Polacek, D. C.; DePaola, N.; Barakat, A. I. Spatial Relationships in Early Signaling Events of Flow-Mediated Endothelial Mechanotransduction. *Annu. Rev. Physiol.* **1997**, *59*, 527−549.
(18) Lindken, R.; Rossi, M.; Große, S.; Westerweel, J. Micro-Particle Image Velocimetry (μPIV): Recent Developments, Applications, and Guidelines. *Lab Chip* **2009**, *9*, 2551−2567.
(19) Santiago, J. G.; Wereley, S. T.; Meinhart, C. D.; Beebe, D.; Adrian, R. J. A Particle Image Velocimetry System for Microfluidics. *Exp. Fluids* **1998**, *25*, 316−319.
(20) Bottier, M.; Blanchon, S.; Pelle, G.; Bequignon, E.; Isabey, D.; Coste, A.; Escudier, E.; Grotberg, J. B.; Papon, J.-F.; Filoche, M.; Louis, B. A New Index for Characterizing Micro-Bead Motion in a Flow Induced by Ciliary Beating: Part I, Experimental Analysis. *PLoS Comput. Biol.* **2017**, *13*, e1005605.
(21) Dabiri, D.; Pecora, C. *Particle Tracking Velocimetry*; IOP Publishing Bristol, 2020.
(22) Dessalles, C. A.; Ramón-Lozano, C.; Babataheri, A.; Barakat, A. I. Luminal Flow Actuation Generates Coupled Shear and Strain in a Microvessel-on-Chip. *Biofabrication* **2022**, *14*, 015003.
(23) Papaioannou, T. G.; Stefanadis, C. Vascular Wall Shear Stress: Basic Principles and Methods. *Hellenic J. Cardiol.* **2005**, *46*, 9−15.
(24) Chistiakov, D. A.; Orekhov, A. N.; Bobryshev, Y. V. Effects of Shear Stress on Endothelial Cells: Go with the Flow. *Acta Physiol.* **2017**, *219*, 382−408.
(25) Lafaurie-Janvore, J.; Antoine, E. E.; Perkins, S. J.; Babataheri, A.; Barakat, A. I. A Simple Microfluidic Device to Study Cell-Scale Endothelial Mechanotransduction. *Biomed. Microdevices* **2016**, *18*, 63.
(26) Kim, J.; Michelin, S.; Hilbers, M.; Martinelli, L.; Chaudan, E.; Amselem, G.; Fradet, E.; Boilot, J.-P.; Brouwer, A. M.; Baroud, C. N.; Peretti, J.; Gacoin, T. Monitoring the Orientation of Rare-Earth-Doped Nanorods for Flow Shear Tomography. *Nat. Nanotechnol.* **2017**, *12*, 914−919.
(27) Fuller, G. G. *Optical Rheometry of Complex Fluids*; Oxford University Press, 1995.
(28) Reinhardt, U. T.; de Groot, E. L. M.; Fuller, G. G.; Kulicke, W. M. Rheo-Optical Characterization (Flow-Birefringence and Flow-Dichroism) of the Tobacco Mosaic Virus. *Macromol. Chem. Phys.* **1995**, *196*, 63−74.
(29) Alizadehgiashi, M.; Khabibullin, A.; Li, Y.; Prince, E.; Abolhasani, M.; Kumacheva, E. Shear-Induced Alignment of Anisotropic Nanoparticles in a Single-Droplet Oscillatory Microfluidic Platform. *Langmuir* **2018**, *34*, 322−330.
(30) Shrestha, S.; Wang, B.; Dutta, P. Nanoparticle Processing: Understanding and Controlling Aggregation. *Adv. Colloid Interface Sci.* **2020**, *279*, 102162.
(31) Wang, Z.; Kim, J.; Magermans, L.; Corbella, F.; Florea, I.; Larquet, E.; Kim, J.; Gacoin, T. Monazite $LaPO_4$: $Eu^{3+}$ Nanorods as Strongly Polarized Nano-Emitters. *Nanoscale* **2021**, *13*, 16968−16976.
(32) Wang, Z.; Delille, F.; Bartier, S.; Pons, T.; Lequeux, N.; Louis, B.; Kim, J.; Gacoin, T. Zwitterionic Polymers toward the Development of Orientation-Sensitive Bioprobes. *Langmuir* **2022**, *38*, 10512−10519.
(33) Delille, F.; Balloul, E.; Hajj, B.; Hanafi, M.; Morand, C.; Xu, X. Z.; Dumas, S.; Coulon, A.; Lequeux, N.; Pons, T. Sulfobetaine-Phosphonate Block Copolymer Coated Iron Oxide Nanoparticles for Genomic Locus Targeting and Magnetic Micromanipulation in the Nucleus of Living Cells. *Nano Lett.* **2023**, *23*, 5919−5926.
(34) Solomon, M. J.; Spicer, P. T. Microstructural Regimes of Colloidal Rod Suspensions, Gels, and Glasses. *Soft Matter* **2010**, *6*, 1391−1400.
(35) Chaudan, E.; Kim, J.; Tusseau-Nenez, S.; Goldner, P.; Malta, O. L.; Peretti, J.; Gacoin, T. Polarized Luminescence of Anisotropic $LaPO_4$:Eu Nanocrystal Polymorphs. *J. Am. Chem. Soc.* **2018**, *140*, 9512−9517.
(36) Son, Y. Determination of Shear Viscosity and Shear Rate from Pressure Drop and Flow Rate Relationship in a Rectangular Channel. *Polymer* **2007**, *48*, 632−637.
(37) Cerf, R.; Scheraga, H. A. Flow Birefringence in Solutions of Macromolecules. *Chem. Rev.* **1952**, *51*, 185−261.
(38) Philippoff, W. Flow Birefringence and Stress. *J. Appl. Phys.* **1956**, *27*, 984−989.
(39) Cressely, R.; Hocquart, R.; Wydro, T.; Decruppe, J. P. Numerical Evaluation of Extinction Angle and Birefringence in Various Directions as a Function of Velocity Gradient. *Rheol. Acta* **1985**, *24*, 419−426.
(40) Gabriel, J.-C. P.; Davidson, P. New Trends in Colloidal Liquid Crystals Based on Mineral Moieties. *Adv. Mater.* **2000**, *12*, 9−20.
(41) Wang, Z.; Senden, T.; Meijerink, A. Photonic Effects for Magnetic Dipole Transitions. *J. Phys. Chem. Lett.* **2017**, *8*, 5689−5694.
(42) Haynes, W. M.; Lide, D. R.; Bruno, T. J. *CRC Handbook of Chemistry and Physics*; CRC Press, 2016.
(43) Dambrine, J.; Géraud, B.; Salmon, J.-B. Interdiffusion of Liquids of Different Viscosities in a Microchannel. *New J. Phys.* **2009**, *11*, 075015.
(44) Perktold, K.; Thurner, E.; Kenner, T. Flow and Stress Characteristics in Rigid Walled and Compliant Carotid Artery Bifurcation Models. *Med. Biol. Eng. Comput.* **1994**, *32*, 19−26.
(45) Duraiswamy, N.; Jayachandran, B.; Byrne, J.; Moore, J. E.; Schoephoerster, R. T. Spatial Distribution of Platelet Deposition in Stented Arterial Models under Physiologic Flow. *Ann. Biomed. Eng.* **2005**, *33*, 1767−1777.
(46) Scheraga, H. A. Relation Between Extinction Angle and Molecular Size. *Arch. Biochem. Biophys.* **1951**, *33*, 277−281.
(47) Calabrese, V.; Varchanis, S.; Haward, S. J.; Shen, A. Q. Alignment of Colloidal Rods in Crowded Environments. *Macromolecules* **2022**, *55*, 5610−5620.
(48) Mahto, S. K.; Tenenbaum-Katan, J.; Greenblum, A.; Rothen-Rutishauser, B.; Sznitman, J. Microfluidic Shear Stress-Regulated Surfactant Secretion in Alveolar Epithelial Type II Cells in Vitro. *Am. J. Physiol. Lung Cell. Mol. Physiol.* **2014**, *306*, L672−L683.
(49) Barbee, K. A.; Davies, P. F.; Lal, R. Shear Stress-Induced Reorganization of the Surface Topography of Living Endothelial Cells Imaged by Atomic Force Microscopy. *Circ. Res.* **1994**, *74*, 163−171.
(50) Flitney, E. W.; Kuczmarski, E. R.; Adam, S. A.; Goldman, R. D. Insights into the Mechanical Properties of Epithelial Cells: the Effects of Shear Stress on the Assembly and Remodeling of Keratin Intermediate Filaments. *FASEB J.* **2009**, *23*, 2110−2119.
(51) Cross, S. E.; Jin, Y.-S.; Rao, J.; Gimzewski, J. K. Biomechanics and Biophysics of Cancer Cells. *Nat. Nanotechnol.* **2007**, *2*, 780−783.


https://doi.org/10.1021/acsnano.4c09493
*ACS Nano* XXXX, XXX, XXX−XXX